ACS MEASUREMENT SCIENCE Au
AN OPEN ACCESS JOURNAL OF THE AMERICAN CHEMICAL SOCIETY

pubs.acs.org/measureau
Article

Gas–Liquid–Solid Three-Phase Boundary in Scanning Electrochemical Cell Microscopy

Published as part of ACS Measurement Science Au special issue "2024 Rising Stars".

C. Hyun Ryu,[‖] Debasree Mandal,[‖] and Hang Ren*

Cite This: *ACS Meas. Sci. Au* 2024, 4, 729–736
Read Online

ACCESS | Metrics & More | Article Recommendations | Supporting Information

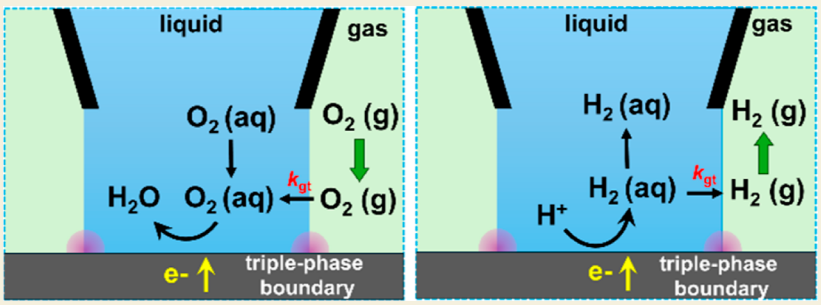

ABSTRACT: The gas–liquid–solid interface plays a crucial role in various electrochemical energy conversion devices, including fuel cells and electrolyzers. Understanding the effect of gas transfer on the electrochemistry at this three-phase interface is a grand challenge. Scanning electrochemical cell microscopy (SECCM) is an emerging technique for mapping the heterogeneity in electrochemical activity; it also inherently features a three-phase boundary at the nanodroplet cell. Herein, we quantitatively analyze the role of the three-phase boundary in SECCM involving gas via finite element simulation. Oxygen reduction reaction is used as an example for reaction with a gas reactant, which shows that interfacial gas transfer can enhance the overall mass transport of reactant, allowing measuring current density of several A/cm^2. The hydrogen evolution reaction is used as an example for reaction with a gas product, and fast interfacial gas transfer kinetics can significantly reduce the concentration of dissolved gas near the electrode. This helps to measure electrode kinetics at a high current density without the complication of gas bubble formation. The contribution of interfacial gas transfer can be understood by directly comparing its kinetics to the mass transfer coefficient from the solution. Our findings aid the quantitative application of SECCM in studying electrochemical reactions involving gases, establishing a basis for investigating electrochemistry at the three-phase boundary.

KEYWORDS: *gas exchange, scanning electrochemical probe microscopy, oxygen reduction reaction, hydrogen evolution reaction, triple phase boundary, nanoelectrochemistry*

1. INTRODUCTION

Electrochemical energy conversion devices, such as fuel cells and electrolyzers, rely heavily on the efficiency of reactions occurring at the electrochemical interface.[1] The architecture of the electrode is often a membrane electrode assembly, which involves a gas–solid–liquid interface, also known as the triple-phase boundary (TPB). At TPB, the gas phase, liquid electrolyte, and solid electrode meet, which is crucial for the efficiency of electrochemical reactions involving gas species.[2] In fuel cells, for example, this TPB is key in electrocatalytic activity because it is the primary location at each electrode, where H_2 and O_2 gases undergo concerted phase transfer and electron transfer.[3] For electrolyzers in which gas is the product, bubbles formed on the electrode also create a three-phase boundary, affecting the efficiency of electrolyzers. However, understanding the dynamics of interfacial gas transfer at the TPB remains a significant challenge due to the complexity and lack of appropriate model systems.[4]

Scanning electrochemical cell microscopy (SECCM) has emerged as a powerful tool for investigating the heterogeneity in electrochemical activity on the nanoscale.[5−7] Unlike bulk electrochemical techniques, SECCM isolates a nanoscopic patch of a macroelectrode by nanodroplet, which enables local electrochemical measurement.[8−11] The fast mass transport in the nanopipette allows for studying fast electrode kinetics.[12,13]

Received: August 17, 2024
Revised: October 3, 2024
Accepted: October 4, 2024
Published: October 10, 2024

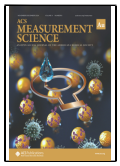

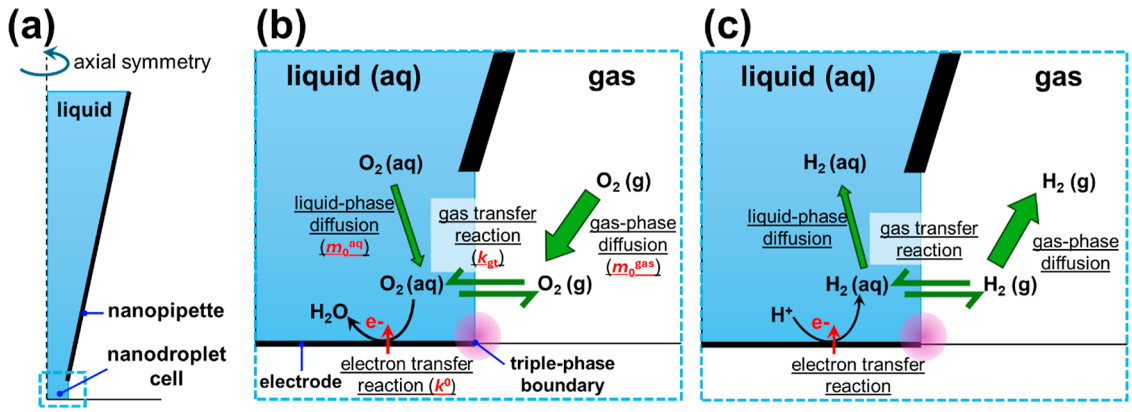

Figure 1. (a) Finite element model for electrochemical reactions involving gas in an SECCM setup, which features a solid−liquid−gas TPB. (b) Electrode reaction involving gaseous reactant, e.g., the O_2 reduction reaction. (c) Electrode reaction involving gaseous product, e.g., the H_2 evolution reaction.

One important feature of SECCM is its TPB. In SECCM, the gas−liquid interface at the droplet is close to the electrode, which enhances the coupling between the interfacial gas transfer reaction and the electron transfer reaction. Therefore, SECCM offers some unique advantages for studying electrochemical reactions involving gas, which constitutes a large class of reactions in electrocatalysis, e.g., hydrogen evolution reaction (HER), hydrogen oxidation reaction, oxygen reduction reaction (ORR), oxygen evolution reaction, and CO_2 reduction reaction.[13−15] For instance, SECCM has been effectively used to study ORR, where the mass transfer of the reactant is significantly enhanced compared to traditional methods like rotating disk electrode.[16] This allows measuring a high current density of ORR.[14,17] On the other hand, efficient gas transfer can effectively remove the gas product at the electrode surface.[14,17,18] This mitigates the problem of bubble formation at high current densities, which allows accurate kinetics measurement without electrode blockage or convective mixing caused by bubble formation and detachment.[19] In addition, the presence of a three-phase interface at the droplet in SECCM presents an opportunity and model system for electrochemistry at the TPB.

While some work has previously acknowledged the role of the interfacial gas-transfer reaction, quantitatively elucidating how the kinetics of this phase transfer reaction affects the electrochemical measurement in SECCM is lacking.[20] In this manuscript, we quantify the effect of the interfacial gas transfer reaction in SECCM and separately treat the electrochemical reactions with a gas product and a gas reactant. Finite element simulation is used to quantify how gas transfer kinetics at the gas−liquid interface affect electrochemical measurement in SECCM, especially voltammetry. Lastly, we discuss the competition between interfacial gas transfer and bulk liquid-phase diffusion.

2. THEORY AND MODEL

2.1. Thermodynamics and Kinetics for the Gas Transfer Reaction

Generally, gas transfer at the gas−liquid interface can be divided into three steps. For example, for gas molecules to transfer from the liquid phase to the gas phase, the first step is mass transport, which moves the molecules from the bulk of the liquid to the interface, often by diffusion. The second step is phase transfer of the gas molecule from the liquid to the gas phase. The microscopic steps of the phase transfer reaction can be complicated due to the dynamic fluctuation of the interface, adsorption, and desolvation of the solute.[21,22] However, we can treat the rate of gas crossing the interface from liquid to gas by first-order kinetics

$$J_{l-g} = k_{l-g} C_A^{liquid} \tag{1}$$

where J_{l-g} is the flux of gas transferred from the liquid phase to the gas phase, k_{l-g} is the corresponding heterogeneous rate constant for gas transfer, and C_A^{liquid} is the concentration of A in the liquid phase at the interface. Similarly, the flux of molecules going into the liquid phase from the gas phase at the interface (J_{g-l}) can be described as

$$J_{g-l} = k_{g-l} C_A^{gas} \tag{2}$$

Similarly, k_{g-l} is the corresponding first-order rate constant, and C_A^{gas} is the concentration of gas A in the gas phase near the interface. At equilibrium, $J_{l-g} = J_{g-l}$, the kinetics reduce to partition equilibrium

$$K_P = \frac{C_A^{liquid}}{C_A^{gas}} = \frac{k_{g-l}}{k_{l-g}} \tag{3}$$

where K_p is the partition coefficient of gas between the liquid and gas phases. Once the molecule enters the gas phase, it can undergo gas-phase mass transport. In principle, any of the three steps can be the rate-limiting step. However, because diffusion in the gas phase is generally 1000 to 10,000 times faster than the liquid phase, mass transport in the gas phase is generally not rate-limiting. This fast gas-phase diffusion can greatly accelerate the transport of molecules through the three-phase interface, which we will discuss in the following sections.

2.2. Finite Element Model

Finite element simulation was used to quantitatively predict the effect of the gas transfer reaction on the voltammetric response. The geometry and the details of the simulation are described in Figure S1 and Supporting Information Section S1. The model contains two phases: a liquid phase (i.e., aqueous electrolyte in our study) and a gas phase, as shown in Figure 1a. The electrochemical reaction (i.e., electron transfer reaction) occurs at the electrode−electrolyte interface, described by the Butler−Volmer formalism with a standard rate constant k^0. We studied two types of reactions; one

https://doi.org/10.1021/acsmeasuresciau.4c00061
ACS Meas. Sci. Au 2024, 4, 729−736

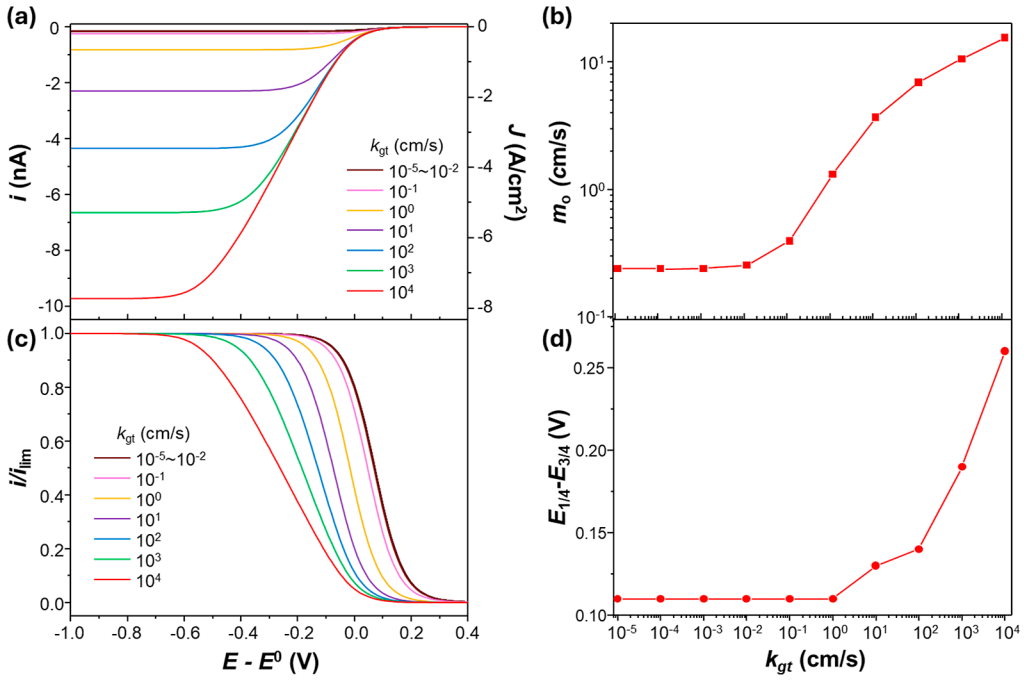

Figure 2. (a) Voltammograms of the ORR reaction at various k_{gt}. (b) Mass transfer coefficient (m_0) as a function of k_{gt}. The standard rate constant for electron transfer (k^0) is 1 cm/s for each simulation. (c) Voltammograms normalized to the limiting current (i_{lim}) at various k_{gt}. (d) Difference in $E_{1/4}$ and $E_{3/4}$ with different k_{gt}.

involves a gaseous reactant entering the solution from the gas–liquid interface, and the other involves a gaseous product generated at the electrode surface exiting the gas–liquid interface. For the former case, we use the ORR to illustrate. As shown in Figure 1b, the gaseous reactant (i.e., O_2) can be transported to the electrode surface from the bulk solution in the pipette via liquid-phase diffusion and from the gas phase through gas transfer reaction at the gas–liquid interface. Effectively, the overall rate of mass transport is the sum of both liquid-phase diffusion and the interfacial gas-transfer reaction (vide infra), which affects the fastest rate of electron transfer (k^0) accessible in steady-state voltammetry.

The second type of reaction involves gaseous products; an example is the HER, as shown in Figure 1c. Similar to the ORR, the key processes involve gas transfer, electron transfer, and mass transfer in the liquid and gas phases. The difference is that the primary role of mass transfer and gas transfer is to remove the gaseous product, H_2, from the electrode. Note that we apply the Butler–Volmer equation to the HER and ORR, assuming that the rate-determining elementary step involves the transfer of one electron.

3. RESULTS AND DISCUSSION

3.1. Effect of Gas Transfer on the Electrochemical Reaction with a Gas Reactant

We use finite element simulation to study the effect of the TPB on the voltammetric response for electrode reactions with the gaseous reactant. The ORR is used as an example reaction to illustrate without losing generality, where 1 atm O_2 in the gas phase can enter the electrolyte at the gas–liquid interface and is reduced at the electrode surface (Figure 1b). The flux of O_2 entering the droplet ($J_{O_2}^{g-l}$) represents the difference between J_{g-l} and J_{l-g} as

$$J_{O_2}^{g-l} = k_{gt}(C_{O_2}^{gas}\kappa_H^{O_2}RT - C_{O_2}^{liquid}) \quad (4)$$

In eq 4, k_{gt} is the rate constant for interfacial gas transfer, $\kappa_H^{O_2}$ is Henry's law constant for O_2, $C_{O_2}^{liquid}$ is the oxygen concentration at the boundary of liquid-phase, $C_{O_2}^{gas}$ is that of gas-phase, R is the gas law constant, and T is temperature. Figure 2a shows the simulated voltammogram for the ORR at different k_{gt}. The limiting current density for ORR remains essentially constant (~−0.12 A/cm²) when k_{gt} is <10^{-2} cm/s, but increases as k_{gt} increases above 10^{-1} cm/s. A wide range of k_{gt} values was chosen in the simulation (10^{-5} to 10^{4} cm/s) to evaluate how gas-transfer kinetics can affect the overall mass transport and voltammetric response without losing generality. For the O_2/water interface, k_{gt} of 0.68 cm/s was reported by Unwin and co-workers.[23] Although the gas–liquid–solid interface is the focus of this report, the model can be directly applied to the liquid–liquid-solid interface in SECCM, which is relevant in the case of "oil-immersion" SECCM.[24]

To help understand the effect of k_{gt} on the voltammogram, the overall mass transfer coefficient (m_0) is calculated from the limiting current via

$$m_0 = \frac{i_{lim}}{nFAC^*} \quad (5)$$

In this equation, n = 4 is the number of electrons transferred per O_2 reduced. F is Faraday's constant. A is the area of the electrode, and C^* is the bulk concentration of the reactant (equals 1.3 mM at 1 atm O_2). The effect of k_{gt} on m_0 is summarized in Figure 2b. When k_{gt} is below 10^{-2} cm/s, m_0 remains constant (~0.24 cm/s). This value is the same as the mass transfer coefficient by liquid-phase diffusion only (i.e., diffusion in the nanopipette and droplet in the absence of gas-transfer reaction), which is termed m_0^{liquid}. In other words, when $k_{gt} \ll m_0^{liquid}$, m_0 is dominated by m_0^{liquid} and is unaffected by k_{gt}. Note that the liquid-phase mass transport in SECCM is already

https://doi.org/10.1021/acsmeasuresciau.4c00061
ACS Meas. Sci. Au 2024, 4, 729–736

fast even without gas transfer, as a rotation rate of approximately 7 × 10^4 rpm would be needed to achieve the same m_0 (see Supporting Information Section S2 for the calculation). When $k_{gt} \gg m_0^{aq}$, the mass transfer is dominated by interfacial gas transfer at the TPB. In this scenario, the overall mass transport increases with k_{gt} (Figure 2b).

The increase in overall mass transfer by the interfacial gas transfer means that SECCM can achieve much higher current density before reaching the mass transfer limit, which was experimentally demonstrated by Dinca and co-workers.[16] In the simulation, a current density of up to 7.8 A/cm^2 can be obtained for the ORR when k_{gt} is 10^4 cm/s (Figure 2a). This also suggests faster electron transfer kinetics can be measured in SECCM for reactions involving gas reactants due to enhanced mass transport. As shown in the normalized voltammograms in Figure 2c, the shape of the voltammogram for the gas transfer reaction can be affected by the interfacial gas transfer when it contributes to the overall mass transfer. When $k_{gt} > m_0^{liquid}$, the voltammetric shape is unaffected by k_{gt}. When k_{gt} is comparable or larger than m_0^{liquid}, the voltammetric curve appears broader as k_{gt} increases, i.e., the current takes a wider potential range to rise to the mass transport limit. This is quantitatively characterized by the Tomeš potential separation, i.e., the difference in the potentials 1/4 and 3/4 of the limiting current, which are termed $E_{1/4}$ and $E_{3/4}$, respectively.[25] As shown in Figure 2d, the Tomeš potential separation remains 110 mV when k_{gt} is smaller than 1 cm/s but continues to increase at larger k_{gt}. Note that we only considered the cathodic part of ORR in the simulation. Therefore, the Tomes criterion (e.g., the characteristic 56 mV potential difference for the reversible voltammogram) does not apply here.

This effect of k_{gt} on the mass transfer of the reactant can be further visualized by inspecting the concentration profiles of O_2. The simulation was performed using irreversible Butler–Volmer kinetics at sufficiently large overpotentials when ORR occurs at the mass transfer limited rate. When k_{gt} is small (e.g., 10^{-5} cm/s), the diffusion layer of O_2 in the droplet extends into the nanopipette, while the concentration of O_2 in the gas phase is not perturbed (Figure 3). As k_{gt} increases, the diffusion layer thickness in the liquid phase decreases due to the supplement of O_2 from the gas phase through interfacial gas transfer. At k_{gt} = 10^4 cm/s, the O_2 concentration in the nanopipette is essentially unperturbed and remains close to the bulk value of ∼1.3 mM, which suggests interfacial gas transfer contributes to most of the O_2 flux. The effect of the geometry of the pipette and droplet on the overall voltammogram is shown in Figures S2–S4.

The effect of gas transfer on the overall mass transfer can be further quantified by dissecting the total flux into those from liquid diffusion (pipette flux) and gas transfer (interfacial flux). As shown in Figure 4, when k_{gt} is low (<0.001 cm/s), overall mass transport of O_2 is controlled by liquid-phase diffusion (pipette flux). The contribution from interfacial transfer to the total flux increases as k_{gt} increases. The interfacial flux constitutes 50% of the total flux when k_{gt} is 0.13 cm/s (Figure 4b), which occurs when k_{gt} is comparable to m_0^{aq}.

3.2. Effect of Gas Transfer on the Electrochemical Reaction with a Gas Product

We now discuss the effect of gas transfer reaction on electrochemical reaction with gas product (e.g., HER) in SECCM. Without interfacial gas transfer, the gas product, e.g., H_2, is transported away from the electrode surface through liquid-phase diffusion to the bulk solution. In the presence of a gas–liquid interface in proximity, the gas product can also cross this interface and enter the gas phase. To understand how the kinetics of the interfacial gas transfer reaction affect the electrochemical response, we simulated the voltammograms for HER in SECCM configuration with different k_{gt}. Unlike in the ORR, the limiting current for HER remains unchanged regardless of k_{gt} because the interfacial gas transfer does not affect the mass transport of the reactant, which determines the limiting current (Figure 5a). However, the voltammetric shape can be affected by the kinetics of gas transfer. It has been suggested that the mass transport of H_2 often limits the fastest kinetics of HER that can be measured.[26] The simulation results show that when k_{gt} is smaller than 10^{-3} cm/s, the voltammogram has the same shape and is unaffected by interfacial gas transfer. This is because the mass transport of H_2 is dominated by the liquid-phase diffusion. Also, because the electron transfer rate constant, k^0 (1 cm/s), is comparable to m_0 (0.862 cm/s), the voltammogram is quasi-reversible, as indicated by the ∼76 mV difference between $E_{1/4}$ and $E_{3/4}$.[25]

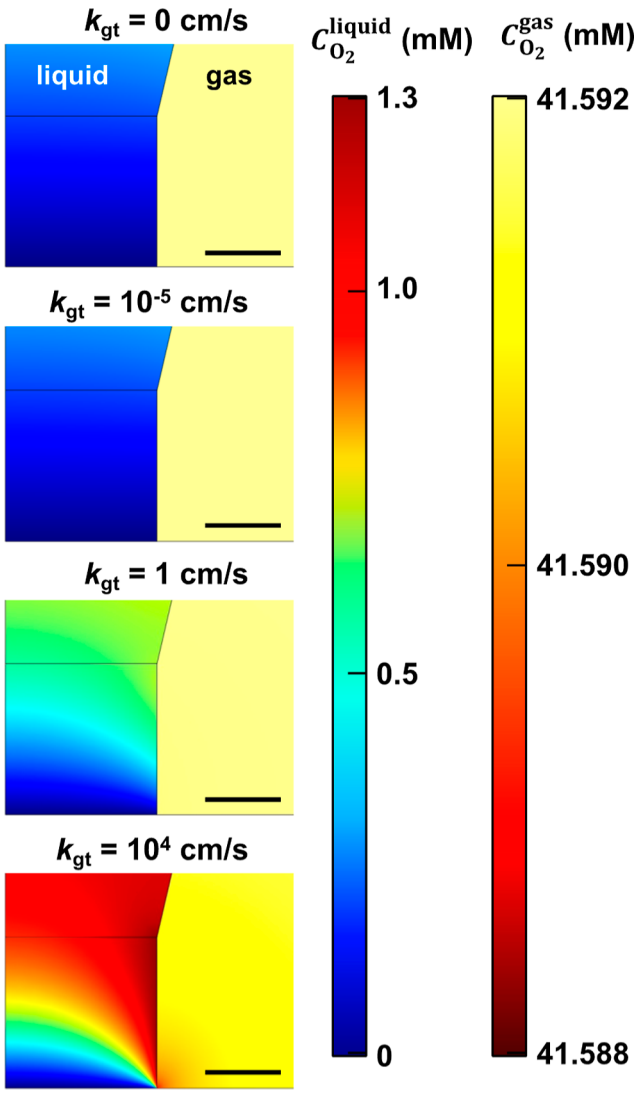

Figure 3. Concentration profiles of O_2 in solution ($C_{O_2}^{liquid}$) and gas phase ($C_{O_2}^{gas}$) for k_{gt} of 0, 10^{-5}, 1, and 10^4 cm/s. −1 V vs E^0 was applied in the simulation. Only the zoomed-in region near the droplet is shown. Scale bars: 100 nm.

https://doi.org/10.1021/acsmeasuresciau.4c00061
ACS Meas. Sci. Au 2024, 4, 729–736

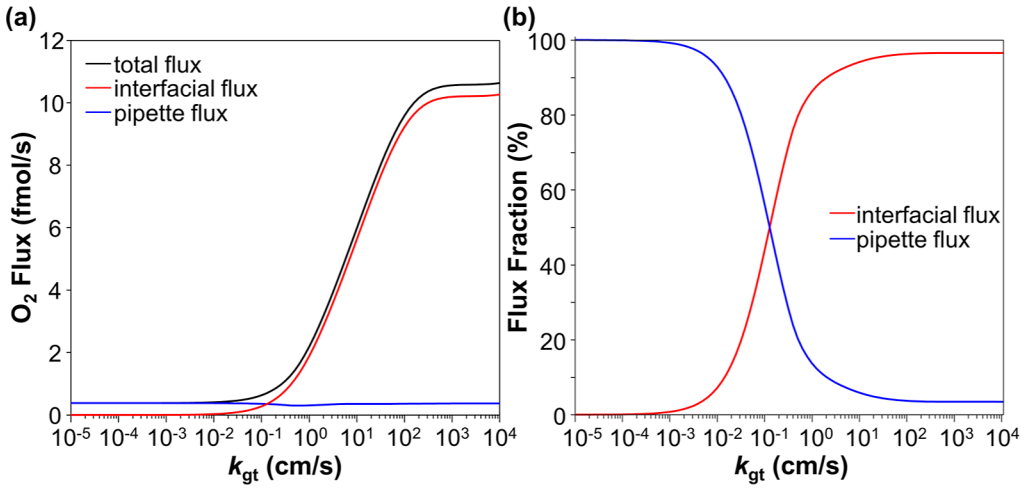

Figure 4. Contribution of interfacial gas transfer vs diffusion in liquid toward the total flux in O_2 reduction. (a) Total O_2 flux to the electrode (total, black), and the partial flux from the interfacial gas transfer (interfacial, red) and liquid diffusion through the pipette (pipette flux, blue) at various gas transfer coefficients (k_{gt}). (b) Percentage of O_2 flux from the interface (red) vs liquid diffusion (blue). The simulation is performed at a potential where oxygen reduction is under mass transfer control (−1 V vs E^0). k^0 = 1 cm/s.

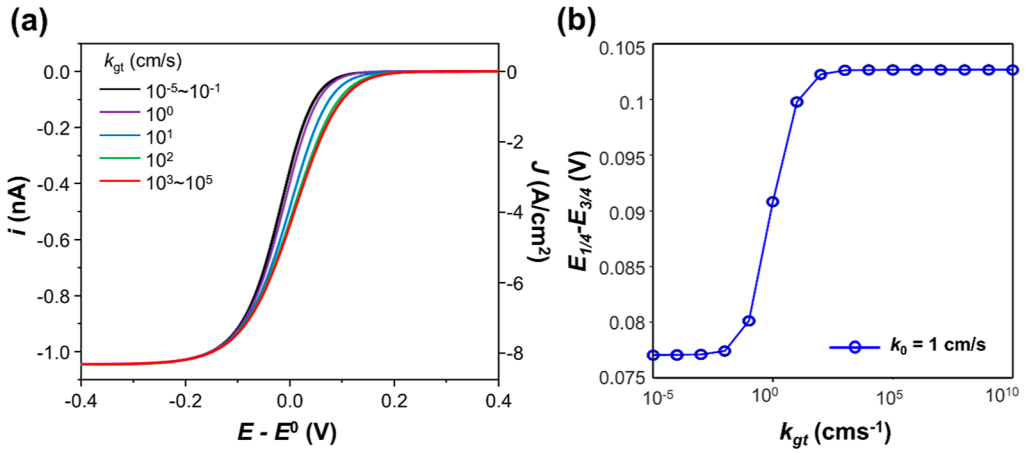

Figure 5. (a) Voltammograms for HER at various k_{gt}. (b) Potential difference in the voltammogram, $E_{1/4} - E_{3/4}$, at different k_{gt}. The standard rate constant for electron transfer (k^0) is 1 cm/s.

When k_{gt} is greater than 10^{-1} cm/s, the voltammetric shape starts to change as the HER onsets at a more positive potential (Figure 5a). This is understood qualitatively as the following. The net current observed is the sum of the cathodic current (from proton reduction) and the anodic current (from H_2 oxidation). More effective removal of H_2 near the electrode from a faster interfacial gas transfer (i.e., larger k_{gt}) reduces the contribution of H_2 oxidation to the net current, shifting the onset potential of HER. Interestingly, $|E_{1/4} - E_{3/4}|$ shifts from ∼76 to ∼102 mV when the kinetics of gas transfer increases (Figure 5b), suggesting a transition from reversible to quasi-reversible voltammogram. The simulated voltammograms $E_{1/2}$ and $E_{1/4} - E_{3/4}$ as a function of k_{gt} at other k^0 are shown in Figures S5 and S6.

Another advantage of the fast transport of gas products by the interfacial gas transfer is that it reduces the surface concentration of dissolved gas near the electrode surface, which is essential for preventing gas bubble nucleation in electrochemical gas evolution reactions.[19] This effect can be visualized in the simulated concentration profile when the current reaches i_{lim}, as shown in Figure 6a. As k_{gt} increases from 10^{-3} to 10^3 cm/s, the H_2 concentration in the solution near the electrode surface decreases dramatically. The maximum concentration of H_2 in the solution ($C_{H_2}^{max}$) at different k_{gt} values under diffusion-limited proton reduction is shown in Figure 6b. At small k_{gt} ($k_{gt} < 10^{-2}$ cm/s), $C_{H_2}{}^{max}$ approaches ∼11 mM, which is the expected surface concentration of H_2 without gas transfer reaction, as calculated by $\frac{C_{H^+}^* D_{H^+}}{2D_{H_2}}$, where C_{H^+}*, D_{H^+}, and D_{H_2} are the bulk H^+ concentration, diffusion coefficient for H^+, and diffusion coefficient for H_2, respectively, all in the liquid phase. This expression can be derived from mass conservation at the electrode surface. However, $C_{H_2}{}^{max}$ is reduced to ∼1 mM when k_{gt} is greater than 1 cm/s. This result suggests that SECCM enables measuring electrode kinetics with the gas product at a higher current density by mitigating bubble formation, which requires a critical concentration for nucleation. Bubble formation at the electrode surface can block the active sites and make it difficult to interpret the electrochemical intrinsic kinetics of gas evolution reactions at high current density.[19,29] White and co-workers used single nanobubble formation on nanoelectrodes to show that H_2 bubble nucleation requires a critical concentration for H_2 of

https://doi.org/10.1021/acsmeasuresciau.4c00061
ACS Meas. Sci. Au 2024, 4, 729−736

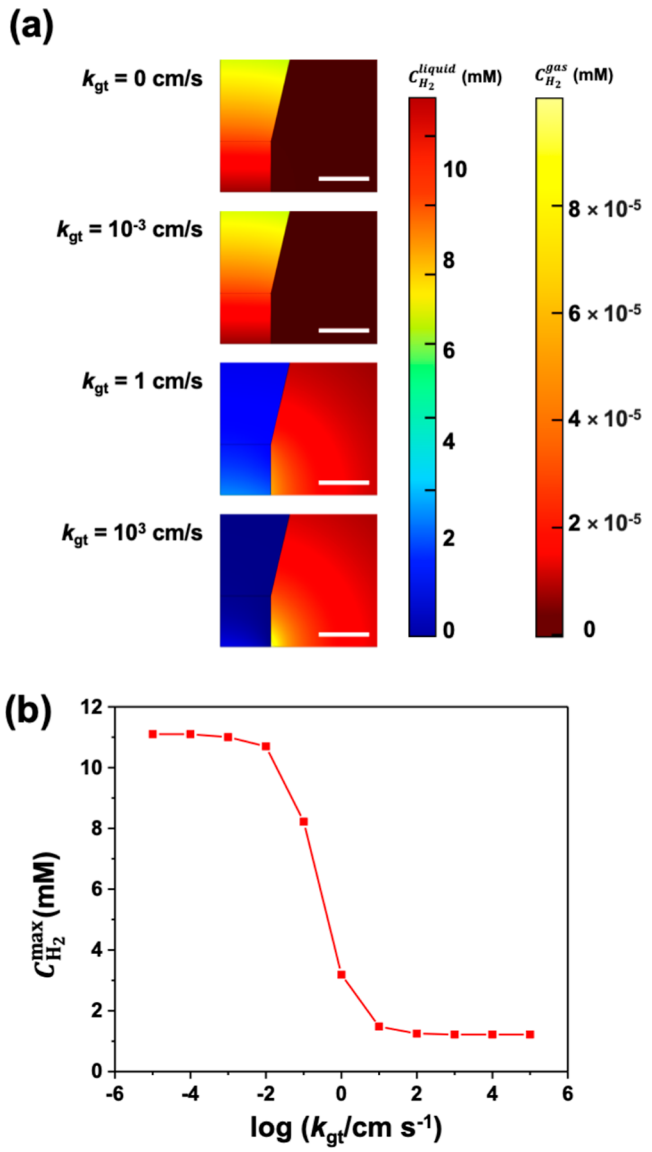

Figure 6. (a) Concentration profiles of H_2 in solution ($C_{H_2}^{liquid}$) and gas phase ($C_{H_2}^{gas}$) for k_{gt} 0, 10^{-3}, 1, and 10^{3} cm/s. Scale bars are 200 nm. (b) Maximum concentration of H_2 within the droplet at various k_{gt}. The standard rate constant (k^0) is 1 cm/s, and the bulk concentration of H^+ is 10 mM.

~250 mM.[27,28] A near 10-fold decrease in the maximum H_2 concentration under SECCM suggests no bubble formation will occur at the mass transport limit even at close to 1 M acid, which we have experimentally shown previously.[17] Note that the maximum concentration of H_2 is also affected by the geometry of the nanopipette/nanodroplet (vide infra), as shown in Figures S7−S9.

Lastly, we investigate how the contribution of interfacial gas transfer changes with the size of the nanopipette/nanodroplet. As illustrated in Figure 1b,c, liquid-phase diffusion and interfacial gas transfer determine the overall mass transfer. When the pipette/droplet size becomes smaller, the diffusion length between the electrode surface and the gas−liquid interface becomes shorter, favoring interfacial gas transfer. Meanwhile, when the droplet size decreases, the area of the gas−liquid interface decreases while the liquid-phase mass transfer coefficient increases. To quantify the overall effect of pipette/droplet size, we evaluated the bulk vs interfacial flux (similar to that shown in Figure 4) at various pipette radii and obtained the critical k_{gt} at which the partial fluxes from interfacial transfer and liquid diffusion are the same. As shown in Figures 7 and S10, critical k_{gt} decreases as the pipette radius increases for both HER and ORR. In other words, the overall contribution of interfacial gas transfer in the SECCM setup increases as the pipette radius increases. This can be understood by considering the mass transfer coefficient from the nanopipette (i.e., liquid diffusion), which describes the mass transport purely in the liquid phase without interfacial gas transfer. We observe a perfect linear correlation between m_0^{liquid} and critical k_{gt}, suggesting the competition can readily be understood by these two characteristic rates. When the pipette size is small, m_0^{liquid} is large, favoring liquid-phase transport through the nanopipette. Therefore, reaching equal contributions from liquid-phase diffusion and interfacial gas transfer needs a higher k_{gt}.

The maximum concentration of H_2 can be affected by the nanopipette size. As shown in Figure 8a, when k_{gt} is small (<10^{-3} cm/s), the bulk diffusion dominates at all the pipette radii investigated (0 to 500 nm); therefore, $C_{H_2}^{max}$ remains ~11 mM regardless of pipette size. Under this scenario, the mass transport of H_2 is dominated by liquid phase diffusion. When k_{gt} is large (>10^{3} cm/s), $C_{H_2}^{max}$ also remains constant, but is reduced to ~1 mM regardless of the pipette radius (between 0 and 500 nm). In this case, the mass transport of H_2 is dominated by the interfacial gas transfer. At the intermediate k_{gt} (10^{-2} to 10^{2} cm/s), increasing pipette size leads to a decrease in $C_{H_2}^{max}$. This is understood similarly by comparing the characteristic rate of liquid-phase diffusion (m_0^{liquid}) vs interfacial gas transfer (k_{gt}). Increasing the radius will decrease m_0^{liquid}, favoring interfacial gas transfer and reducing the dissolved gas concentration near the electrode. The concentration profiles at different pipette radii for k_{gt} = 0.01 cm/s are shown in Figure 8b. Consistent with the statement above that a larger pipette radius favors interfacial gas transfer over bulk mass transport, the concentration of H_2 in the gas phase just outside the droplet increases with the pipette radius. Additionally, the maximum concentration of proton is scaled linearly with proton concentration at different k_{gt} (Figure S11).

4. CONCLUSIONS

In conclusion, the role of the gas transfer reaction in electrochemical measurement involving gas as a reactant or product is studied using finite element simulation in the context of SECCM, where a solid−liquid−gas phase interface naturally exists at the active electrode. Using ORR as an example of a reaction involving a gas reactant, we showed that the limiting current increases with the kinetics of the gas transfer reaction of O_2, suggesting that the interfacial gas transfer reaction can greatly increase mass transfer. This increase in mass transfer of reactant allows measurement of the ORR at high current density and fast electrochemical kinetics. When gas is the product of an electrochemical reaction (e.g., H_2 in HER), the kinetics of the interfacial gas transfer reaction affect the maximum concentration of dissolved gas species at a given current. The simulation shows that the maximum surface concentration of H_2 in the HER can be reduced by a factor of 10. This allows the measurement of HER kinetics under high current density without the complication of bubble formation at the electrode under SECCM, which is difficult to obtain in

https://doi.org/10.1021/acsmeasuresciau.4c00061
ACS Meas. Sci. Au 2024, 4, 729−736

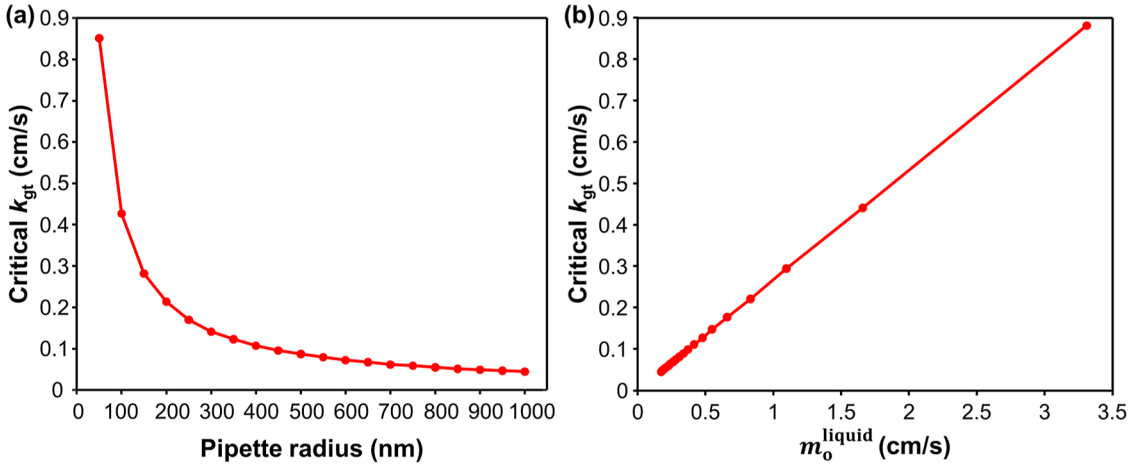

Figure 7. Effect of pipette radius on the critical k_{gt} at which the fluxes from liquid-phase diffusion and interfacial gas transfer are equal. (a) Critical k_{gt} as a function of pipette radius for HER. (b) Critical k_{gt} as a function of the liquid phase mass transfer coefficient (m_0^{liquid}).

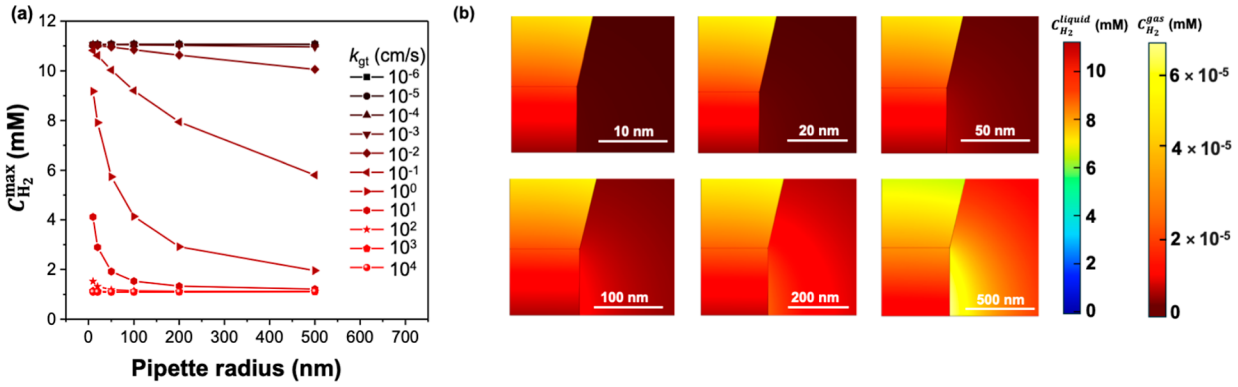

Figure 8. (a) Maximum H_2 concentration in the droplet vs nanopipette radius at different k_{gt}. (b) H_2 concentration profile within the droplet and air for different nanopipette radii at k_{gt} = 0.01 cm/s.

conventional electrochemical measurement. Both effects can be understood by comparing the characteristic rate constants of bulk mass transfer and interfacial gas transfer. Lastly, the study is based on continuum theory without explicitly addressing the kinetics-coupled electron- and phase−transfer reaction at the three-phase boundary. However, our study serves as a baseline for investigating and interpreting the unique electrochemistry at the three-phase boundary.

5. METHODS

Finite element simulations were performed using the transport of dilute species module in COMSOL Multiphysics. Two-dimensional axial geometry was used to represent the geometry of the pipette and droplet in SECCM. Gas-phase and liquid-phase diffusion were treated in two transport of dilute species modules, which are coupled at the interface by the flux described by eq 4. Maximum mesh element size was 0.4 nm at the three-phase interface. A detailed description of the simulation geometry and boundary conditions can be found in Supporting Information Section S1 and can also be found in the COMSOL model reports as part of the Supporting Information.

■ ASSOCIATED CONTENT

Supporting Information

The Supporting Information is available free of charge at https://pubs.acs.org/doi/10.1021/acsmeasuresciau.4c00061.

Finite element model, examples of voltammograms, mass transfer coefficient calculation in RDE, effect of pipette/droplet geometry, and effect of bulk proton concentration (PDF)

COMSOL model report for HER (PDF)

COMSOL model report for ORR (PDF)

■ AUTHOR INFORMATION

Corresponding Author

Hang Ren − *Department of Chemistry, The University of Texas at Austin, Austin, Texas 78712, United States; Center for Electrochemistry and Texas Materials Institute, The University of Texas at Austin, Austin, Texas 78712, United States;* orcid.org/0000-0002-9480-8881; Email: hren@utexas.edu

Authors

C. Hyun Ryu − *Department of Chemistry, The University of Texas at Austin, Austin, Texas 78712, United States;* orcid.org/0000-0001-8656-3581

Debasree Mandal − *Department of Chemistry, The University of Texas at Austin, Austin, Texas 78712, United States*

Complete contact information is available at: https://pubs.acs.org/10.1021/acsmeasuresciau.4c00061

Author Contributions

‖C.H.R. and D.M. contributed equally. CRediT: **C. Hyun Ryu** conceptualization, data curation, formal analysis, writing -

https://doi.org/10.1021/acsmeasuresciau.4c00061
ACS Meas. Sci. Au 2024, 4, 729−736

original draft, writing - review & editing; **Debasree Mandal** data curation, formal analysis, writing - original draft, writing - review & editing; **Hang Ren** conceptualization, data curation, funding acquisition, investigation, supervision, writing - review & editing.

Notes

The authors declare no competing financial interest.

■ ACKNOWLEDGMENTS

The authors would like to acknowledge support from the Chemical Measurement & Imaging (CMI) Program at the National Science Foundation (CHE-2240113). The facility used at the Center for Electrochemistry is supported by the Welch Foundation (H−F-0037).

■ REFERENCES

(1) Stamenkovic, V. R.; Strmcnik, D.; Lopes, P. P.; Markovic, N. M. Energy and Fuels from Electrochemical Interfaces. *Nat. Mater.* **2017**, *16* (1), 57−69.

(2) Wang, Y.-C.; Huang, W.; Wan, L.-Y.; Yang, J.; Xie, R.-J.; Zheng, Y.-P.; Tan, Y.-Z.; Wang, Y.-S.; Zaghib, K.; Zheng, L.-R.; Sun, S.-H.; Zhou, Z.-Y.; Sun, S.-G. Identification of the Active Triple-Phase Boundary of a Non-Pt Catalyst Layer in Fuel Cells. *Sci. Adv.* **2022**, *8* (44), No. eadd8873.

(3) O'Hayre, R.; Prinz, F. B. The Air/Platinum/Nafion Triple-Phase Boundary: Characteristics, Scaling, and Implications for Fuel Cells. *J. Electrochem. Soc.* **2004**, *151* (5), A756−A762.

(4) Weng, C.-C.; Lv, X.-W.; Ren, J.-T.; Ma, T.-Y.; Yuan, Z.-Y. Engineering Gas-Solid-Liquid Triple-Phase Interfaces for Electrochemical Energy Conversion Reactions. *Electrochem. Energy Rev.* **2022**, *5* (S1), 19.

(5) Daviddi, E.; Shkirskiy, V.; Kirkman, P. M.; Robin, M. P.; Bentley, C. L.; Unwin, P. R. Nanoscale Electrochemistry in a Copper/Aqueous/Oil Three-Phase System: Surface Structure-Activity-Corrosion Potential Relationships. *Chem. Sci.* **2021**, *12* (8), 3055−3069.

(6) Ryu, C. H.; Lee, H.; Lee, H.; Ren, H. Learning from the Heterogeneity at Electrochemical Interfaces. *J. Phys. Chem. Lett.* **2022**, *13* (33), 7838−7846.

(7) Ebejer, N.; Schnippering, M.; Colburn, A. W.; Edwards, M. A.; Unwin, P. R. Localized High Resolution Electrochemistry and Multifunctional Imaging: Scanning Electrochemical Cell Microscopy. *Anal. Chem.* **2010**, *82* (22), 9141−9145.

(8) Bentley, C. L.; Kang, M.; Unwin, P. R. Nanoscale Structure Dynamics within Electrocatalytic Materials. *J. Am. Chem. Soc.* **2017**, *139* (46), 16813−16821.

(9) Lee, H.; Matthews, K. C.; Zhan, X.; Warner, J. H.; Ren, H. Precision Synthesis of Bimetallic Nanoparticles via Nanofluidics in Nanopipets. *ACS Nano* **2023**, *17* (22), 22499−22507.

(10) Yule, L. C.; Shkirskiy, V.; Aarons, J.; West, G.; Shollock, B. A.; Bentley, C. L.; Unwin, P. R. Nanoscale Electrochemical Visualization of Grain-Dependent Anodic Iron Dissolution from Low Carbon Steel. *Electrochim. Acta* **2020**, *332*, 135267.

(11) Li, M.; Ye, K.-H.; Qiu, W.; Wang, Y.; Ren, H. Heterogeneity between and within Single Hematite Nanorods as Electrocatalysts for Oxygen Evolution Reaction. *J. Am. Chem. Soc.* **2022**, *144* (12), 5247−5252.

(12) Anderson, K. L.; Edwards, M. A. Evaluating Analytical Expressions for Scanning Electrochemical Cell Microscopy (SECCM). *Anal. Chem.* **2023**, *95* (21), 8258−8266.

(13) Chen, C.-H.; Meadows, K. E.; Cuharuc, A.; Lai, S. C. S.; Unwin, P. R. High Resolution Mapping of Oxygen Reduction Reaction Kinetics at Polycrystalline Platinum Electrodes. *Phys. Chem. Chem. Phys.* **2014**, *16* (34), 18545−18552.

(14) Wang, Y.; Li, M.; Ren, H. Voltammetric Mapping of Hydrogen Evolution Reaction on Pt Locally via Scanning Electrochemical Cell Microscopy. *ACS Meas. Sci. Au* **2022**, *2* (4), 304−308.

(15) Ryu, C. H.; Ren, H. Simultaneous Mapping of Electrocatalytic Activity and Selectivity via Hybrid Scanning Electrochemical Probe Microscopy. *Nano Lett.* **2024**, *24* (20), 6112−6116.

(16) Mariano, R. G.; Wahab, O. J.; Rabinowitz, J. A.; Oppenheim, J.; Chen, T.; Unwin, P. R.; Dinca, M. Thousand-Fold Increase in O_2 Electroreduction Rates with Conductive MOFs. *ACS Cent. Sci.* **2022**, *8* (7), 975−982.

(17) Wang, Y.; Gordon, E.; Ren, H. Mapping the Nucleation of H_2 Bubbles on Polycrystalline Pt via Scanning Electrochemical Cell Microscopy. *J. Phys. Chem. Lett.* **2019**, *10* (14), 3887−3892.

(18) Tetteh, E. B.; Kim, M.; Savan, A.; Ludwig, A.; Chung, T. D.; Schuhmann, W. Reassessing the Intrinsic Hydrogen Evolution Reaction Activity of Platinum Using Scanning Electrochemical Cell Microscopy. *Cell Rep. Phys. Sci.* **2023**, *4* (12), 101680.

(19) Zhao, X.; Ren, H.; Luo, L. Gas Bubbles in Electrochemical Gas Evolution Reactions. *Langmuir* **2019**, *35* (16), 5392−5408.

(20) Deng, X.; Shan, Y.; Meng, X.; Yu, Z.; Lu, X.; Ma, Y.; Zhao, J.; Qiu, D.; Zhang, X.; Liu, Y.; Chen, Q. Direct Measuring of Single-Heterogeneous Bubble Nucleation Mediated by Surface Topology. *Proc. Natl. Acad. Sci. U.S.A.* **2022**, *119* (29), No. e2205827119.

(21) Rane, K. Fluctuations and Adsorption at Liquid-Vapor Interfaces. In *Physical Chemistry of Gas−Liquid Interfaces*; Faust, J. A., House, J. E., Eds.; Developments in Physical & Theoretical Chemistry; Elsevier, 2018; Chapter 3, pp 59−78.

(22) Nathanson, G. M.; Davidovits, P.; Worsnop, D. R.; Kolb, C. E. Dynamics and Kinetics at the Gas-Liquid Interface. *J. Phys. Chem.* **1996**, *100* (31), 13007−13020.

(23) Slevin, C. J.; Ryley, S.; Walton, D. J.; Unwin, P. R. A New Approach for Measuring the Effect of a Monolayer on Molecular Transfer across an Air/Water Interface Using Scanning Electrochemical Microscopy. *Langmuir* **1998**, *14* (19), 5331−5334.

(24) Li, Y.; Morel, A.; Gallant, D.; Mauzeroll, J. Oil-Immersed Scanning Micropipette Contact Method Enabling Long-Term Corrosion Mapping. *Anal. Chem.* **2020**, *92* (18), 12415−12422.

(25) Bard, A. J.; Faulkner, L. R.; White, H. S. *Electrochemical Methods: Fundamentals and Applications*; John Wiley & Sons, 2022.

(26) Sheng, W.; Gasteiger, H. A.; Shao-Horn, Y. Hydrogen Oxidation and Evolution Reaction Kinetics on Platinum: Acid vs Alkaline Electrolytes. *J. Electrochem. Soc.* **2010**, *157* (11), B1529.

(27) German, S. R.; Edwards, M. A.; Ren, H.; White, H. S. Critical Nuclei Size, Rate, and Activation Energy of H_2 Gas Nucleation. *J. Am. Chem. Soc.* **2018**, *140* (11), 4047−4053.

(28) Luo, L.; White, H. S. Electrogeneration of Single Nanobubbles at Sub-50-Nm-Radius Platinum Nanodisk Electrodes. *Langmuir* **2013**, *29* (35), 11169−11175.

(29) Amatore, C.; Savéant, J. M.; Tessier, D. Charge Transfer at Partially Blocked Surfaces: A Model for the Case of Microscopic Active and Inactive Sites. *J. Electroanal. Chem. Interfacial Electrochem.* **1983**, *147* (1), 39−51.

https://doi.org/10.1021/acsmeasuresciau.4c00061
ACS Meas. Sci. Au 2024, 4, 729−736